



HAL
open science

Enhancement of the photocatalytic response of Cu-doped TiO₂ nanotubes induced by the addition of strontium

W. Alrashedi, H. Kochkar, G. Berhault, M. Younas, A. Ben Ali, N.A.
Alomair, R. Hamdi, S.A. Abubshait, O. Alagha, M.F. Gondal, et al.

► **To cite this version:**

W. Alrashedi, H. Kochkar, G. Berhault, M. Younas, A. Ben Ali, et al.. Enhancement of the photocatalytic response of Cu-doped TiO₂ nanotubes induced by the addition of strontium. *Journal of Photochemistry and Photobiology A: Chemistry*, 2022, 428, pp.113858. 10.1016/j.jphotochem.2022.113858 . hal-03842495

HAL Id: hal-03842495

<https://hal.science/hal-03842495>

Submitted on 7 Nov 2022

HAL is a multi-disciplinary open access archive for the deposit and dissemination of scientific research documents, whether they are published or not. The documents may come from teaching and research institutions in France or abroad, or from public or private research centers.

L'archive ouverte pluridisciplinaire **HAL**, est destinée au dépôt et à la diffusion de documents scientifiques de niveau recherche, publiés ou non, émanant des établissements d'enseignement et de recherche français ou étrangers, des laboratoires publics ou privés.

Enhancement of the Photocatalytic Response of Cu-doped TiO₂ Nanotubes induced by the Addition of Strontium

W. Alrashedi^{1,2}, H. Kochkar^{1,2*}, G. Berhault^{3*}, M. Younas⁴, A. Ben Ali^{1,2}, N.A. Alomair^{1,2}, R. Hamdi², S. A. Abubshait², O. Alagha⁵, M.F. Gondal⁴, M. Haroun⁶, C. Tratat⁶

¹ Department of Chemistry, College of Science, Imam Abdulrahman Bin Faisal University, P.O. Box 1982, 31441, Dammam, Saudi Arabia.

² Basic & Applied Scientific Research Center, Imam Abdulrahman Bin Faisal University, P.O. Box 1982, 31441, Dammam, Saudi Arabia.

³ Institut de Recherches sur la Catalyse et l'Environnement de Lyon, CNRS Université Lyon I, 69100 Villeurbanne, France.

⁴ Department of Physics, College of Sciences, King Fahd University of Petroleum & Minerals, Dhahran, 31261, Saudi Arabia.

⁵ Environmental Engineering Department, College of Engineering, Imam Abdulrahman Bin Faisal University, Dammam 31441, Saudi Arabia

⁶ Department of Pharmaceutical Sciences, College of Clinical Pharmacy, King Faisal University, Al-Ahsa 31982, Saudi Arabia

**Corresponding authors. E-mail addresses: hbkochkar@iau.edu.sa (H. Kochkar)*

Abstract

The influence of adding strontium to Cu-doped TiO₂ nanotubes on the photocatalytic performance of the resulting materials was herein studied considering changes in structural, textural, optical and morphological properties. Addition of strontium was performed in a 0.2-1.0 wt% range while an optimized fixed Cu loading of 0.5 wt% was used. TiO₂ nanotubes were obtained using alkaline hydrothermal treatment of P25 followed by a calcination treatment at 400°C. The resulting TiNT material was then impregnated with copper using an incipient wetness impregnation followed by a new calcination at 400°C (0.5Cu-TiNT). Strontium was then added under similar impregnation-calcination conditions. The effect of adding various amounts onto 0.5Cu-TiNT was therefore deeply characterized using X-ray diffraction, N₂ adsorption-desorption measurements, scanning electron microscopy coupled with energy-dispersive X-ray analysis, Raman, UV-vis diffuse reflectance, X-ray photoelectron, and photoluminescence spectroscopies as well as determining dielectric properties.

Results clearly emphasize that up to a Sr loading of 0.8 wt%, the addition of Sr results in in situ formation of Sr-O-Ti entities on the surface of 0.5Cu-TiNT. Above this threshold loading, excess Sr loading leads to the formation of segregated SrO species. Finally, a direct correlation was observed here between the optimized formation of surface Sr-O-Ti entities and an enhanced

photocatalytic response due to improved stabilization of photogenerated charges on 0.5Cu-TiNT resulting from the ferroelectric interference of neighboring SrTiO₃ entities.

Keywords: Copper; Strontium; TiO₂ nanotube; Photodegradation

Introduction

Photocatalysis is an efficient and sustainable approach generally used to degrade toxic molecules present in wastewater or the atmosphere [1-3]. Its use has also more recently been extended to energy applications (e.g., H₂, C₁ production) or to the transformation of renewable resources (selective photooxidation) [4]. Titanium dioxide (TiO₂) is the most used semiconductor in photocatalysis due to its abundance, good chemical stability, and suitable band edge potentials for H₂ production [5-8]. However, its large band gap (3.2 eV for anatase) restrains its use to photoexcitation under UV illumination. Moreover, TiO₂ presents a very high recombination rate of photogenerated carriers (electron-hole pairs) limiting its intrinsic activity. Different strategies have been used in enhancing the TiO₂ response to photoexcitation limited by electron-hole pairs recombination. One approach is to modify the morphology of TiO₂ nanostructures through the formation of 1D nanoobjects (tubes, rods, wires). This morphological approach is successful to enhance the photocatalytic activity under UV illumination [9-12]. Other options to limit recombination include the addition of other semiconductors to obtain heterojunctions [13-16] or the doping with cations [17-20]. Among the various candidates for TiO₂ doping, copper is a promising choice. Copper has several oxidation states leading to different oxide species on TiO₂ photocatalysts, mainly Cu₂O and CuO. This has led to controversial results about the real nature (CuO or Cu₂O) of the copper oxide species involved in enhancing TiO₂ photocatalytic properties [21-24].

Improved catalytic activities have also been reported by combining TiO₂ with graphene oxide, which can play both the roles of electron acceptor and photosensitizer [25-27]. Moreover, copper doping on graphene oxide with or without TiO₂ was found to be an interesting option for enhanced photocatalytic systems. For instance, Tran et al. studied a copper oxide-reduced graphene oxide composite photocatalyst for hydrogen generation [28]. Similarly, Lv et al. evidenced the synergetic

effect between copper and graphene as cocatalysts on TiO_2 for enhanced photocatalytic hydrogen evolution during solar water splitting [29].

However, all these synthesis methods led to limited success in improving the photocatalytic activity. One way to enhance the efficiency of photocatalytic materials is to develop “assisted” photocatalysis processes. In this respect, charge separation can be driven by the electric field created in the depletion region and from the energy discontinuity at the semiconductor/electrolyte interface. Therefore, tuning the electronic band structure in the interfacial region appears to be a very effective approach to enhance charge separation efficiency. In this respect, ferroelectric polarization is a promising strategy to modify band structures and charge transport performances in heterojunction-based semiconductors. The built-in electric polarization can lead to tremendous free charge redistribution in adjacent semiconductors, effectively tuning the width and amplitude of the depletion region [30-33]. Generating locally such spontaneous polarization by the addition of a ferroelectric material to the photocatalyst can provide a strong opportunity to monitor the charge separation regardless of the synthesis limitations.

Few attempts have been done in the literature to build devices combining ferroelectrics and semiconductor materials by growing the SrTiO_3 phase onto TiO_2 systems. Different methodologies were envisaged like TiO_2 anodization [34] or controlled alkaline hydrothermal treatment (for rutile TiO_2 nanowires) [31]. In situ Sr or Ba substitution was therefore performed under hydrothermal conditions. However, these methods suffer from a low-scale production of anodized TiO_2 materials or the use of inappropriate low active rutile phase. TiO_2 microspheres were also envisaged but their very large size limits the proportion of TiO_2 semiconductor phase influenced by ferroelectric domains [35]. On the contrary, Liu et al. [36] deposited mixed TiO_2 anatase and rutile phases by sol-gel process onto hydrothermally synthesized BaTiO_3 but with limited photoelectric conversion efficiency and poor interfacial control. Generally, improved photocatalytic performances were observed without distinguishing the p-n heterojunction effects from the induced ferroelectric polarization effects.

SrTiO_3 offers favorable conditions for photocatalysis since its conduction band is only 200 mV more negative than TiO_2 . However, the role played by ferroelectricity was rarely considered in this case because SrTiO_3 is generally considered paraelectric [37, 38]. This oversimplified statement was recently ruled out since under optical excitation, SrTiO_3 becomes ferroelectric [39, 40]. Moreover, even stress-free SrTiO_3 materials have been found to present inherent ferroelectric

domains [41]. Consequently, the probability for photocatalytic reaction versus electron-hole recombination will then significantly increase [42]. Such an increase in the local electric field may then benefit from the morphological control of the metal/semiconductor system through the size and shape of the metal particle [43, 44].

The objective herein will be to demonstrate the interest of combining strontium titanate nanoparticles with Cu-doped TiO₂ semiconductors (with optimized 1D morphology) to enhance photocatalytic processes. The first part of this work will be devoted to study the effect of the strontium loading onto 1D TiO₂ nanotubes (NTs) doped with 0.5 wt % Cu. Physicochemical properties of Sr/Cu-NTs nanomaterials will then be correlated with their photocatalytic behaviors.

2. Experimental

2.1. Elaboration of the Photocatalysts

2.1.1. Elaboration of TiO₂ Nanotubes

Titanate nanotubes were obtained using a hydrothermal procedure under strongly alkaline conditions described in our previous works [9, 45, 46]. Typically, 3 g of TiO₂ powder were reacted with 90 mL of a highly concentrated solution of NaOH (11.25 mol.L⁻¹) in a 150 mL Teflon-line autoclave at 130°C for 20 h with a heating rate of 2°C/min. The obtained suspension was filtered. The resulting powder was then neutralized with HCl solution (0.1 mol.L⁻¹) and washed with hot distilled water several times to remove sodium and chloride ions. In order to further eliminate the excess of sodium, a second washing with an HCl solution of higher concentration (1.0 mol.L⁻¹) was carried out. The resulting hydrogenotitanate powder was then dried at 80°C for 12 h. This sample was named HTiNT and corresponds to a hydrogenated H₂Ti₂O₉.H₂O phase [47]. Finally, the HTiNT material was treated for 2 h at 400°C under air (heating ramp: 2°C/min, air flow: 10 mL/min) to convert the hydrogenotitanate phase into TiO₂ anatase. This solid was then named as TiNT.

2.1.2. Elaboration of Sr-doped Cu-TiO₂ Nanotubes

First, TiNT materials were doped with an optimum 0.5 wt% copper amount following an incipient wetness impregnation method as described in [48] using Cu(NO₃)₂.3H₂O (Sigma Aldrich, 99%) as a precursor. The obtained paste was dried in an oven at 80°C for 24 h and then calcined under air at 400°C for 2 h (heating ramp: 2°C/min, air flow: 10 mL/min). The resulting nanomaterials

are named 0.5Cu-TiNT. In a second step, 0.5Cu-TiNT was doped with different amounts of strontium (0.2, 0.4, 0.6, 0.8, and 1.0 wt %) using the same incipient wetness impregnation methodology used previously but with Sr(NO₃)₂ (Sigma Aldrich, 99%). Firstly, the desired strontium loading has been obtained by dissolving strontium nitrate in 1.0 mL aqueous solution. Then the strontium-containing solution is added to 1 g of 0.5Cu-TiNT catalyst. The obtained paste was dried in an oven at 80 °C for 24 h and then calcined under air at 400 °C for 2 h (heating ramp: 2°C/min, air flow: 10 mL/min). Samples were then named as xSr-0.5Cu-TiNT with x the weight percentage of Sr used.

2.2. Catalyst Characterization

Elemental analysis of strontium and copper was performed using Plasma Atomic Emission Spectroscopy (Shimadzu ICPE-9820). The ICP analysis of copper and strontium was carried-out at wavelengths of 324.754 nm and 407.771 nm, respectively. A high-performance microwave procedure was carried out to achieve a shorter digestion time. Typically, 50 mg of 0.5Cu-TiNT or xSr-0.5Cu-TiNT samples were digested with 10 mL of a freshly prepared mixture of concentrated HNO₃–H₂O₂–HF (8.5:1:0.5, v/v). Digestion conditions for the microwave system were applied for 2 hours at 300 W. After cooling; the resulting solutions were diluted 5 times up to 10 mL in volumetric flasks with ultra-high pure water (18 MΩ).

Textural properties of the different photocatalysts were obtained on a Micromeritics ASAP 2020 analyzer using N₂ adsorption-desorption isotherms at 77 K. Specific surface areas were obtained using the Brunauer-Emmett-Teller (BET) method considering the adsorption data branch in the relative P/P₀ pressure range varying between 0.05 and 0.25. The Barrett-Joyner-Halenda (BJH) model was applied for the determination of pore size distributions.

The photocatalysts were structurally characterized using X-ray diffraction (XRD) analysis. XRD data were collected on an automatic diffractometer (Philips Panalytical X'Pert ProMPD) using a Ni-filtered Cu Kα radiation source ($\lambda = 1.54184 \text{ \AA}$). Crystallite sizes were retrieved using the Scherrer equation:

$$L = K\lambda/\beta\cos\theta$$

Where L is the crystallite size, λ the wavelength of X-ray radiation, β the full width at half maximum (FWHM), and K the shape factor (taken as 1 in the present case).

Raman analysis was carried out on a Horiba Jobin Yvon LabRAM-HR equipment. Experiments were made at 20°C in the 100-2500 cm⁻¹ wavenumber range. The spectral resolution was 4 cm⁻¹. Excitation was performed using a 514 nm Ar-Kr RM2018 laser while spectra were recorded using a CCD detector cooled at -75°C. The laser power was fixed at 1 mW at the surface of the samples to avoid radiation damage.

Transmission Electron Microscopy (TEM) was performed on a JEOL 2010 (200 kV) microscope to reveal the morphology of the different samples. The TEM analysis specimens were first dispersed in ethanol before dropwise addition and drying onto a holey carbon film supported on a Cu grid (300 mesh).

UV-vis diffuse reflectance spectroscopy (UV-vis DRS) measurements were performed using an AvaSpec-2048 Fiber Optic instrument with asymmetrical Czerny-Turner design. Spectra were recorded from 250 to 800 nm using a 2048 pixel CCD detector array. Bandgap energy values were evaluated using the Kubelka–Munk method. $F(R)hv^{1/2}$ versus hv plots were built with $F(R) = (1 - R)/2R$, assuming an indirect bandgap transition.

X-ray photoelectron spectroscopy (XPS) studies were carried out using a Thermo Scientific ESCALAB 250Xi equipped with a dual Al/Mg anode and a hemi-spherical analyzer operating at fixed pass energy of 50 eV. A 150 W monochromatic source (Al K α = 1486.6 eV) was used to excite the samples. The samples were pressed on a double sided carbon tape attached to the sample holder and placed into the XPS instrument. Binding energies were obtained with a precision of 1.0 eV. Curve fitting was done using mixed Gaussian and Lorentzian functions for line shaping after treatment of the background using Thermo Avantage software, version 5.51.

Electrochemical impedance spectroscopy (EIS) is a useful technique for studying mobile charge dynamics in interfacial domains. As a function of frequency, the real (Z') and imaginary (Z'') elements of the complex electrical impedance (Z^*) were measured using a Palmsens4 equipment. The experiments were carried out with a 25 mV_{RMS} sinusoidal signal over a frequency range of 1Hz to 1MHz.

2.3 Photocatalytic Experiments

Photocatalytic tests were performed using an aqueous solution (30 cm³) containing different concentrations of formic acid as the reactant molecule to be degraded. Formic acid was used as a representative common intermediate observed during the degradation of many organic compounds comprising carboxylic functions. The reaction was carried out in a Pyrex photoreactor (100 cm³) (optical window area: 12.5 cm²). The concentration of photocatalyst was set at 1.0 g.L⁻¹ for all the samples studied. The pH of the different solutions was close to 3.0 ± 0.5 depending on the formic acid concentration used. A PL-L (18 W) lamp was used for UV irradiation. An optical 0.52 Corning filter was employed to cut-off wavelength below 340 nm. A radiant flux of 5 mW.min⁻¹ was fixed for all experiments. Before UV irradiation, the suspensions were stirred at a given formic acid concentration in the dark for 30 min to reach adsorption equilibrium conditions. The formic acid concentration of the solution after equilibration was then measured and used as the initial concentration (C₀). Formic acid samples were taken for analysis at different intervals (C) from the photoreactor while the photocatalyst was separated from the liquid phase by filtration. Withdrawn samples were then analyzed with a Varian ProStar High-Performance Liquid Chromatograph (HPLC) equipped with a Coregel-87H3 column (300 mm×7.8 mm). A H₂SO₄ (5.10⁻³ mol.L⁻¹) mobile phase was used at a flow rate of 0.7 mL.min⁻¹. Experiments were triplicated for all samples.

3. Results and Discussion

3.1 ICP elemental analysis

The results of elemental ICP analysis of copper and strontium onto 0.5Cu-TiNT and xSr-0.5Cu-TiNT nanomaterials are collected in Table 1. The copper loading is close to the theoretical one (0.5 wt%) and attained an average value of 0.48 ± 0.02 wt%. Similarly, the average strontium impregnation loading is close to the expected ones except for the 1.0Sr-0.5Cu-TiNT with a Sr loading 15% higher experimentally. Hence, the Sr average experimental values onto 0.5Cu-TiNT material agrees with targeted theoretical ones.

3.2 X-ray Diffraction (XRD)

Figure 1A illustrates the X-ray diffraction patterns of Sr-doped xSr-0.5Cu-TiNT materials (with x wt% = 0.2, 0.4, 0.6, 0.8, and 1.0) as well as of the strontium-free 0.5Cu-TiNT and copper-free

TiNT as references. Both 0.5Cu-TiNT and xSr-0.5CuTiNT samples present characteristic XRD peaks corresponding to the anatase phase at 2θ values of 25.4° , 38.1° , 48.3° , 54.0° , 55.1° , and 62.8° ascribed to the (101), (004), (200), (105), (211) and (204) reflections [9]. The comparison between 0.5Cu-TiNT and TiNT (Fig.1B) does not show any shift of the (101) reflection of anatase confirming previous observations about the absence of distortion of bulk TiO_2 induced by copper addition [49, 50]. Moreover, the addition of strontium does not lead to the appearance of new XRD peaks like those expected for SrO. In addition, Sr doping does not induce any shift of the main (101) diffraction peak of the anatase phase, indicating the absence of distortion in the TiO_2 lattice. Strontium, therefore, cannot enter into the lattice of bulk TiO_2 . This can be attributed to the differences in radius and charges between Sr^{2+} (1.18 Å) and Ti^{4+} (0.68 Å). In the present case, the presence of strontium oxide (SrO) or strontium titanate (SrTiO_3) is highly probable even if their corresponding contributions in the XRD patterns of the doped samples cannot be detected. This can be explained by the low strontium content, which is insufficient for XRD detection, or to the fact that strontium is highly dispersed onto the TiO_2 nanotubes. Further characterizations are in progress using synchrotron XRD techniques to deeply determine the structure of Sr-doped TiO_2 entities onto the surface of the xSr-0.5Cu-TiNT materials. Similarly, previous studies have shown that doping TiO_2 with large ionic radius elements like lanthanides (La, Ce, Eu) impacts the anatase crystallite size by generating surface defects like oxygen vacancies [17, 45, 51-57]. Therefore, in the present case, crystallite sizes were determined using the Scherrer equation [58] applied to the (101) plane of the anatase phase. Values for crystallite sizes of the different samples are summarized in Table 2. Anatase crystallite sizes are similar for all the Sr-doped 0.5Cu-TiNT nanomaterials with values around 12.6 ± 0.4 nm showing the absence of crystallite size variation compared to the Sr-free 0.5Cu-TiNT reference (12.6 nm). This could result from the excellent stabilized structural properties of the starting 0.5 Cu-TiNT material, as shown previously [48].

3.3 Textural Properties

The textural properties of the Sr-doped 0.5Cu-TiNT materials were determined using N_2 adsorption-desorption measurement (Figure 2). All solids present type IV isotherm profiles with H3 hysteresis loops at $P/P_0 \sim 0.7$. Such isotherms are characteristic of non-rigid aggregates of particles giving rise to slit-shaped pores [9, 59]. Table 2 reports the textural properties (BET

specific surface areas, pore diameters, porous volumes, and heat of N₂ adsorption) of the different xSr-0.5Cu-TiNT materials. Results show that the specific surface area decreases with increasing Sr loading going from 102 m²/g for 0.5Cu-TiNT to about 70-80 m²/g for the samples containing high Sr loading (0.6-1.0 wt%). However, pore diameter values, as well as pore volumes, only slightly decrease with increasing Sr loading suggesting that intergranular porosity between aggregates of bunched TiO₂ nanotubes induced by Van der Waals interactions is mainly observed here. Therefore, variations do not result from any change in the nanotubular morphology of these TiO₂-based materials [60, 61]. Finally, the evolution of N₂ adsorption heat values evolution does not show any significant variation for the Sr-containing samples compared to the Sr-free reference up to a Sr loading of 0.8 wt% Sr. At the highest Sr loading (1.0Sr-0.5Cu-TiNT), a higher heat of N₂ adsorption was found (3.47 kJ.mol⁻¹), suggesting a modification in the surface interaction with the adsorbate, which may reflect the appearance of separate SrO species.

3.4 Raman Spectroscopy

Raman spectra of the xSr-0.5Cu-TiNT nanomaterials are shown in Figure 3A. Comparison is provided to the Sr-free 0.5Cu-TiNT reference. The Raman signature clearly shows the presence of the TiO₂ anatase phase characterized by an intense contribution at 143 cm⁻¹ due to the E_{1g} vibration mode. At the same time, other anatase bands are also observed at 159 (E_g), 394 (B_{1g}), 514 (B_{1g}/A_{1g}), and 638 cm⁻¹ (E_g). Once again and in agreement with previous XRD observations, no new vibration bands corresponding to additional phases due to strontium or copper addition can be detected even at the highest Sr loading suggesting a very high degree of dispersion of these elements. Moreover, the position of the main E_{1g} mode of anatase (figure 3B) at 142.3 cm⁻¹ on the Sr-free 0.5Cu-TiNT sample shifts to a higher wavenumber of 143.9 cm⁻¹ after the addition of 0.2 wt% Sr. This blue shift has been attributed previously [17, 57] to the appearance of surface oxygen vacancies, which are directly related to the incorporation of Sr species at the TiO₂ surface. However, as soon as a Sr loading of 0.4 wt% is reached, the shift reverses to lower values. This redshift leads to maxima for the main E_{1g} mode of anatase at 143.4, 142.5 and 141.9 cm⁻¹ for 0.4Sr-0.5Cu-TiNT, 0.6Sr-0.5Cu-TiNT and 0.8Sr-0.5Cu-TiNT respectively. This effect was previously assigned to the distortion of the anatase crystalline lattice [62], to a non-uniform distribution of particle sizes [63], or to the appearance of a new phase on the surface of the semiconductor [64]. However, distortion of the

TiO₂ anatase crystalline lattice has been ruled out here using XRD. Moreover, a non-uniform distribution of such low loading of strontium onto a high surface area TiO₂ nanotube is quite improbable. Therefore, this redshift can be assigned to the appearance of other phases like SrTiO₃ or SrO. The fact that already at a low loading of 0.2 wt% in Sr, this element induces the creation of surface oxygen vacancies suggests a strong initial interaction of strontium with TiO₂. This may favor the in-situ formation of SrTiO₃ domains on the surface of the TiO₂ nanotubes. Finally, at 1.0 wt% Sr, the shift moves back to higher wavenumbers with a value going back to 142.5 cm⁻¹ suggesting the appearance of a separate strontium phase like SrO. This would mean that the maximum proportion of in situ formed SrTiO₃ was achieved at 0.8 wt% Sr.

3.5 UV-vis Diffuse Reflectance Spectroscopy

Figure 4 reports the UV-vis diffuse reflectance spectra acquired on the Sr-free 0.5Cu-TiNT and on the different xSr-0.5Cu-TiNT samples (with x in wt% = 0.2, 0.4, 0.6, 0.8, and 1.0). UV-vis DR profiles present a dominant, strong absorption band in the UV region up to 350 nm due to O²⁻(2p) → Ti⁴⁺(3d) charge transfer processes [65]. Moreover, whatever the Sr loading, similar onset values are found, showing that the addition of strontium to the Cu-doped TiO₂ nanotubes does not lead to the incorporation of strontium inside the TiO₂ matrix in agreement with XRD results. To confirm such an assumption, the determination of the bandgap energy (E_g) values using the Kubelka-Munk method was performed considering an indirect bandgap transition as expected for anatase [66]. The resulting Tauc plots are provided in Figure S1, supplementary information, while the determined E_g values are given in Table 2. The addition of strontium does not significantly shift the bandgap with E_g values between 3.41 and 3.45 eV. It should be noted that this absence of E_g shift can be expected if SrTiO₃ is formed at the surface of TiO₂ nanotubes since SrTiO₃ and TiO₂ are known to present similar bandgap values [34, 35, 67]. However, a more detailed analysis also shows the appearance of a new absorbance contribution around 400-450 nm on the xSr-0.5Cu-TiNT samples compared to TiO₂ alone. Moreover, the absorbance intensity of this new contribution does not depend on the Sr loading showing that this feature depends mainly on the addition of copper. Two contributions due to copper can be expected in the visible region: one around 420 nm and another one around 800 nm. The first contribution around 420 nm is generally ascribed either to Cu⁺ 3D clusters in CuO matrix [68-70] or directly to Cu₂O species [65, 71, 72].

The second contribution around 800 nm can be attributed to the d-d transition (${}^2E_g \rightarrow {}^2T_{2g}$) of octahedral Cu^{2+} species [73, 74].

3.6 SEM-EDX Analysis

FESEM images were also acquired on the Sr-free and Sr-containing Cu-doped TiO_2 nanotubes in order to visualize the surface morphology of the photocatalytic materials obtained in this study. Figure 5 shows the FESEM images of the Sr-free 0.5Cu-TiNT (Figures 5a and d) and of the 0.6Sr-0.5Cu-TiNT (Figures 5b and e) and of the 1.0Sr-0.5Cu-TiNT (Figures 5c and f) samples. FESEM images reveal that whatever the Sr loading, similar morphologies were obtained formed of rough aggregates with intergranular porosity. This result confirms an absence of any effect of strontium on the aggregation degree of the photocatalytic material.

Additionally, the elemental composition and surface distribution of the Sr-free 0.5Cu-TiNT, 0.6Sr-0.5Cu-TiNT, and 1.0 Sr-0.5Cu-TiNT samples were determined through EDX analysis (Figure S2) with corresponding Z-elemental mappings (Figure S3). EDX analysis (Figure S2) confirmed the presence of Cu, Ti, and O elements on the Sr-free 0.5Cu-TiNT while Sr was easily detected on 0.6Sr-0.5Cu-TiNT. Elemental mapping, particularly for Cu and Sr, shows that their surface distribution on the photocatalytic samples is quite homogeneous, confirming a quite good dispersion of these elements on the surface of the photocatalysts in agreement with XRD analysis.

3.7 X-Ray Photoelectron Spectroscopy

xSr-0.5Cu-TiNT samples (with x in wt% = 0.2, 0.6 and 1.0) were also analyzed by X-ray photoelectron spectroscopy in comparison to the Sr-free 0.5Cu-TiNT reference (Figure 6).

XPS survey scans (Figure 6A) confirm the presence of signals corresponding to Cu, Ti, O for all samples while the Sr 3d signal at around 135 eV was detected mainly on the 0.6Sr-0.5Cu-TiNT and 1.0Sr-0.5Cu-TiNT samples.

Ti 2p XPS signals were further analyzed, as shown in Figure 6B. Ti 2p core-level spectra gives rise to two Ti 2p_{1/2} and Ti 2p_{3/2} doublets at binding energies around 464.5 eV and 458.7 eV respectively. The Ti 2p_{3/2} signal was further studied by decomposing its signal into two contributions at binding energies of 458.8 eV and 456.7 eV, respectively, for 0.5Cu-TiNT. These

contributions can be attributed to Ti^{4+} and Ti^{3+} species, respectively [65, 75, 76]. Similar decompositions into Ti^{4+} and Ti^{3+} components can be found for the $x\text{Sr}-0.5\text{Cu}-\text{TiNT}$ samples. Respective binding energy values and proportions of Ti^{4+} and Ti^{3+} species are reported in Table 3. The addition of strontium as soon as 0.2 wt% leads to a strong decline of the proportion of Ti^{3+} species from 23.8% for the Sr-free 0.5Cu-TiNT to 10.1% for 0.2Sr-0.5Cu-TiNT. This is accompanied by a significant shift of binding energy to lower values. Indeed, the addition of 1.0 wt% Sr leads to a decrease by 0.5 eV of the Ti^{4+} binding energy contribution from 458.8 to 458.3 eV. This shift to lower binding energy values and the decrease in Ti^{3+} species suggest that surface oxygen vacancies related to the presence of Ti^{3+} moieties are rapidly consumed during the addition of strontium, leading to Ti-O-Sr entities and weakening the Ti-O bond strength correspondingly. High-resolution O 1s XPS core-level spectra were also acquired for the same series of Sr-containing 0.5Cu-TiNT samples and were compared to the Sr-free 0.5 Cu-TiNT reference (Figure 6C and Table 3). O 1s XPS spectrum for 0.5Cu-TiNT presents two contributions at 530.0 eV and 530.6 eV corresponding respectively to lattice oxygen O^{2-} (O_α) species and to adsorbed oxygen (O_β) such as defect-oxide O_2^- or hydroxyl-like OH^- groups [77]. In this respect, in the case of 0.5Cu-TiNT without strontium, the O_α signal shifts to higher energy values compared to the value usually expected (529.5 eV) [78]. This shift is mainly attributed to the formation of oxygen vacancies confirming the formation of these species in higher proportion on 0.5Cu-TiNT. Addition of strontium leads to a shift of the O_α signal to lower binding energy values by about 0.5 eV in the case of 1.0Sr-0.5Cu-TiNT, confirming that surface oxygen vacancy associated with Ti^{3+} species are rapidly consumed when strontium is added. This is accompanied by a fast decrease of the proportion of O_β species, implying that hydroxyl-like groups were probably consumed here to form Ti-O-Sr entities.

High-resolution X-ray photoelectron spectra were also recorded at the Cu 2p core level (Figure 6D). Cu^{2+} species generally present a main Cu $2p_{3/2}$ signal at a binding energy value 1.3 ± 0.2 eV higher than metallic Cu or Cu^+ species [79, 80]. It should be noted that the Cu $2p_{3/2}$ mainline does not present a sufficient binding energy shift to differentiate Cu^+ from Cu^0 species. Moreover, the Cu LMM Auger peak tends to overlap with the Ti 2s XPS peak making the Auger signal useless for distinguishing between Cu^+ and Cu^0 . However, Cu^{2+} species present significant satellite peaks on the high binding energy side of the main Cu $2p_{3/2}$ peak with two shake-up signals at 6 and 8 eV

above the Cu 2p principal line. These shake-up satellite peaks are not observed in our case showing that copper oxidation degree was +I (or 0).

Moreover, the main Cu 2p_{3/2} peak tends to shift to higher binding energy when strontium is added from 932.1 to 932.2, 932.4, and 932.6 eV when going respectively from 0.5Cu-TiNT to 0.2Sr-0.5Cu-TiNT, 0.6 Sr-0.5Cu-TiNT and finally 1.0Sr-0.5Cu-TiNT. This shift suggests some electronic perturbation of copper species related to the Sr addition. Additionally, the intensity of the Cu 2p_{3/2} mainline slightly decreases for the 1.0Sr-0.5Cu-TiNT sample suggesting some surface covering of copper species by strontium at high Sr loading, which might be associated to the formation of SrO entities in plus of Sr-O-Ti species at this high strontium loading.

High-resolution Sr 3d core level region only presents low resolved XPS signals (Figure S4) for which the two Sr 3d_{3/2} and Sr 3d_{5/2} doublets are not deconvoluted. For the 0.2 Sr-0.5Cu-TiNT sample, the Sr 3d signal is hardly detectable while the Sr 3d intensity increases strongly up to 0.6Sr-0.5Cu-TiNT. The intensity only marginally further increases for 1.0Sr-0.5Cu-TiNT, showing that maximum surface dispersion of strontium on the Cu-doped TiO₂ nanotubes is achieved between 0.6 and 1.0 wt% Sr loading. Even if not resolved into two doublets, the optimum of the Sr 3d signal is observed at 134.5 eV for 0.6 Sr-0.5Cu-TiNT, which corresponds to the average value between Sr 3d_{3/2} and Sr 3d_{5/2} signals expected for Sr²⁺ species in SrTiO₃ [81, 82]. Moreover, the onset of the Sr 3d signal on the high binding energy side for 1.0Sr-0.5Cu-TiNT sample shifts from about 137.0 to 138.5 eV, suggesting the possible appearance of a second contribution due to Sr oxide in agreement with the study made by Bourlier et al. [83] about the appearance of SrO contribution on SrVO₃ films.

The XPS analysis, therefore, reveals a net modification of the Ti, O, and Sr species with increasing addition of Sr onto Cu-doped TiO₂ nanotubes. Surface oxygen vacancies associated to Ti³⁺ species tend to be progressively consumed, leading to the formation of SrTiO₃ entities, while for high Sr loading (1.0 wt%), additional formation of strontium oxide entities can be noticed.

3.8 Photoluminescence Spectroscopy

Photoluminescence (PL) spectra were also acquired for the same series of xSr-0.5Cu-TiNT samples with x = 0.2, 0.4, 0.8 and 1.0 (Figure 7). Results were recorded using an excitation source centered at 330 nm while spectra are herein presented in the 350-700 nm wavelength range.

Several emission processes can be noticed on the PL curves. The main emission peaks can be divided into four groups: 1) around 380 nm, this UV emission contribution results from phonon-assisted indirect transition from the edge (X) to the center (Γ) of the Brillouin zone [45, 84], 2) the contribution around 490 nm related to charge transfer processes from Ti^{3+} species to TiO_6^{2-} octahedra [85], 3) one more important peak detected at 440 nm and attributed to bulk recombination between self-trapped electrons and holes [86, 87], and finally 4) emission peaks at around 465 and 550 nm due to recombination of photoelectrons but this time with surface oxygen defects [87]. The analysis of PL results shows that whatever the Sr loading, the photoluminescence profiles present similar contributions whose relative proportions remain unchanged when increasing the Sr content. However, one should note for the 0.4Sr-0.5Cu-TiNT sample, a slightly higher intensity for the 440 nm contribution but a lower one for the 550 nm emission peak. This evolution remains, however, marginal. The main effect observed is a decrease in the PL profiles intensity above a 0.4 wt% Sr loading with similar intensities for 0.8Sr-0.5Cu-TiNT and 1.0Sr-0.5Cu-TiNT. However, this decrease in intensity is not accompanied by a modulation of the proportion of each emission peak. This suggests that increasing the Sr loading above 0.4 wt% leads to a general loss of photoluminescence and, therefore, a lower tendency for recombination inside the TiO_2 bulk lattice or with surface oxygen vacancies. One should then conclude that increasing the Sr content leads to a lower propensity for recombination but independently of any structural modification of the intrinsic optical properties of the TiO_2 -based materials.

3.9 Photocatalytic tests

In order to obtain further information on the influence of adding strontium to Cu-doped TiO_2 nanotubes on their respective photocatalytic properties, formic acid photodegradation tests were performed under UV-A irradiation. TiNT, 0.5Cu-TiNT and the series of xSr-0.5Cu-TiNT samples (x in wt% = 0.2, 0.4, 0.6, 0.8, and 1.0) were investigated. Formic acid (FA) was chosen as a representative example of many organic molecules acting as pollutants and containing carboxylic functions since FA is the last intermediate before complete mineralization into CO_2 . The evolution of FA concentration in the function of the reaction time for the different samples is reported in Figure 8, while initial degradation rates are compiled in Table 4.

Results clearly underlined that the strontium addition strongly enhanced the photocatalytic response of the Cu-doped TiO₂ nanotube systems. First of all, one should note that adding 0.5 wt% Cu to the TiO₂ nanotubes leads to a significant improvement of the photodegradation rate by 40% compared to the TiO₂ nanotubes alone. Previous experimental observations [48] made by combining PL, Raman and X-ray photoelectron spectroscopies clearly underlined that the heterojunction found between TiO₂ and Cu₂O in the present case results in a net transfer of photogenerated electrons from TiO₂ to Cu₂O under UV irradiation. This fact combined with the respective expected band structure energy levels for these two semiconductors [88] militates for the formation of an S-scheme heterojunction in which electrons generated on TiO₂ recombined with the holes from the VB of Cu₂O leaving powerful photogenerated electrons and holes respectively in Cu₂O and TiO₂ [89] and explaining the high gain in photoactivity observed here. This improvement is even more remarkable if the comparison is made with the P25 reference. Adding strontium leads to a progressive enhancement of the photocatalytic response with almost a linear improvement up to a strontium loading of 0.8 wt% as shown in Figure 9. The activity observed at the optimum for 0.8Sr-0.5Cu-TiNT is 40% higher than for 0.5Cu-TiNT and 91% higher than for TiO₂ nanotubes alone. When compared to P25, the activity enhancement reaches 151%.

Interestingly, when the Sr loading was further increased to 1.0 wt% Sr, the activity decreased markedly with an initial degradation rate of about 42 $\mu\text{mol.L}^{-1}.\text{min}^{-1}$ similar to what was observed for the TiO₂ nanotubes alone showing a complete loss of the beneficial effect from both Cu and Sr. This beneficial enhancement of the photooxidation ability of Sr-Cu containing TiO₂ nanotubes up to a Sr loading of 0.8 wt% correlates well with preceding characterization results which show an optimum in the formation of Sr-O-Ti entities on the TiO₂ nanotube surface at a Sr content of 0.8 wt%, optimum associated with a general decrease in the intensity of the PL spectra above 0.6 wt% Sr. Therefore, results emphasize well that the formation of SrTiO₃ species on the TiO₂ nanotube surface up to a Sr loading of 0.8 wt% is the main cause for achieving a beneficial effect on the photocatalytic response. Similarly, increasing further the Sr loading to 1.0 wt% revealed a change in the nature of the Sr species formed with the appearance of SrO species partially covering the copper nanoparticles and canceling any beneficial effect from both SrTiO₃ or copper. One should now determine the causes behind the photocatalytic enhancement observed when adding strontium through the formation of Sr-O-Ti entities. Preceding results acquired by Raman, XPS,

and PL spectroscopies all confirm the role played here by the in-situ formation of Sr-O-Ti or SrTiO₃ domains on the TiO₂ surface. Interestingly, PL results showed only a general decrease in PL intensity without any modification of the relative contributions responsible for photoluminescence. This suggests that the role of strontium is not related to a change in the relative contributions of electron-hole pair phenomena inside the bulk versus the capture of photoelectrons by surface oxygen vacancies, contrary to what was observed in our previous studies [17, 45, 46]. Another possibility would be related to a ferroelectric contribution coming from the in-situ formation of SrTiO₃ entities on the TiO₂ surface and allowing a better separation of photogenerated charges through their stabilization at the semiconductor surface, making them more available for the production of reactive oxygen species (ROS) able to degrade the formic acid molecules.

The role of ferroelectricity in (Ba,Sr)TiO₃ systems adjacent to TiO₂ or other semiconductors was already envisaged by several authors [31-33]. Moreover, even if bulk SrTiO₃ is generally paraelectric, lattice distortion resulting for instance from the in-situ generation of SrTiO₃ domains at the surface of another oxide semiconductor can generate ferroelectric properties. Indeed, recent results have reconsidered SrTiO₃ as a metastable paraelectric compound for which mechanical, electric or optical perturbations can change its paraelectric state to a ferroelectric one [39, 41, 90].

3.10 Dielectric properties

In order to further analyze a possible role of ferroelectricity in the beneficial enhancement observed through the in-situ formation of Sr-O-Ti entities, the determination of dielectric properties was performed in this section using electrochemical impedance spectroscopy (EIS) considering a low Sr-containing sample (0.2Sr-0.5Cu-TiNT) and the 0.8 Sr-0.5Cu-TiNT sample for which the optimum in photocatalytic degradation was observed. On the opposite, the 0.2Sr-0.5Cu-TiNT sample presents an activity only about 10% higher than the 0.5Cu-TiNT reference, while previous characterization results showed that the of Sr-O-Ti species was limited in this case. An impedance analyzer (PalmSens) was used to perform frequency-dependent impedance measurements for the two different samples (0.2Sr-0.5Cu-TiNT and 0.8Sr-0.5Cu-TiNT) pelletized with a 13 mm diameter and a 2 mm thickness. Samples were then placed between two glasses coated with conductive FTO electrodes. The complex impedance measurements were carried out at room temperature by scanning the frequency from 0.1Hz to 1MHz with a voltage of 0.5 V. In

Figure 10, the electrical response of the material was represented using a Nyquist diagram (spectra of the real part and the imaginary part of the complex impedance, Z^* ($Z^* = Z' + jZ''$; $j^2 = -1$), as a function of the exciting frequency). Scattered experimental points are arranged in an approximately circular arc. This response can be associated with an electric dipole formed by resistance in parallel with a capacitor. However, since the scattered points do not form exactly half circles, a model combining only resistance with a capacitor element is insufficient to describe EIS results accurately. Hence, a Constant Phase Element (CPE) in parallel with a resistance R is usually regarded as a better representation of the circuit-fitting parameters [91]. The equivalent electrical circuit of the samples is shown in the inset of Figure 10. The red line represents the best fit. The total impedance of the circuit is given by:

$$Z^* = ReZ^* + ImZ^* = Z' + jZ'' = \left(\frac{1}{R} + \frac{1}{Z_{CPE}^*} \right)^{-1}$$

where the impedance of the CPE is defined via [92]:

$$Z_{CPE}^* = \frac{1}{A_0(j\omega)^n}$$

where ω is the angular frequency ($\omega = 2\pi f$), A_0 is a constant independent of frequency [93], and $0 < n < 1$ is a dimensionless parameter determining the degree of deviation from an exact semicircle [94]. When $n = 1$, Eq. (2) yields the impedance of a capacitor, where $A_0 = C$. The resistance R is the intercept of the impedance curve with Z' Axis. The experimental semicircles have been fitted by the ORIGINLAB software based on the following relationships.

$$Z' = \frac{R \left(1 + RA_0\omega^n \cos\left(\frac{n\pi}{2}\right) \right)}{1 + 2RA_0\omega^n \cos\left(\frac{n\pi}{2}\right) + (RA_0\omega^n)^2}$$

$$Z'' = \frac{R^2 A_0 \omega^n \sin\left(\frac{n\pi}{2}\right)}{1 + 2RA_0\omega^n \cos\left(\frac{n\pi}{2}\right) + (RA_0\omega^n)^2}$$

Figure 10 shows that the same types of curves were obtained. The maximum imaginary impedance spectra Z'' is shifted to high frequency, with increasing the percentage of Sr. It shows that increasing the Sr loading induces a decreasing of the capacitance C and an increase of the time constant τ and on the resistance R. The extracted parameters from the fit for the circuit elements

are collected in Table 5. For each loop, a time constant τ (lifetime at the depletion layer of the semiconductor) equal to the product of the resistance and the capacitance associated with that loop is defined.

Going from 0.2Sr-0.5Cu-TiNT to 0.8Sr-0.5Cu-TiNT leads to an increase of the resistance from 350 K Ω to 948 K Ω while the electron lifetime increases from 199.9 μ s to 355.3 μ s. On the opposite, the capacitance tends to decrease from 571.3 pF to 374.8 pF. Since the probability for an electron to recombine with a hole is generally considered to increase with the decrease of τ , i.e. the time the electron spends in the depletion layer at the semiconductor surface, this would normally mean that the recombination of electron-hole pairs would be enhanced when the percentage of Sr is increased. However, the assumption that increasing the time spent by an electron in the depletion layer would increase the probability for this electron to recombine with a hole is in contradiction with the previous photocatalytic results showing an enhanced photocatalytic response at the Sr loading of 0.8 wt%. Another way to define the τ parameter would be to consider it as the time required to charge or discharge the capacitor within a certain percentage of its full supply since the energy charging (storage) and discharging (release) of a capacitor is never instantaneous. This means that the τ parameter also reflects the time that photogenerated charges remain available at the semiconductor interface for generating reactive oxygen species able to degrade formic acid. The fact that photogenerated charges can remain 75% longer at the semiconductor interface without inducing higher recombination between holes and electrons confirms a better availability of these excitons for reacting directly or indirectly (through ROS formation) with formic acid. This better availability also results from a higher stabilization of these photogenerated charges directly related to the formation of Sr-O-Ti entities inducing a net polarization of the semiconductor surface. In this respect, ferroelectric domains induced by these in situ formed Sr-O-Ti entities would then play a beneficial role in stabilizing photogenerated charges on the oxide semiconductor surface while limiting their potential recombination.

4. Conclusion

In the present study, the addition of low amounts of strontium to Cu-doped TiO₂ nanotubes was herein studied in order to determine its potential role in enhancing the photooxidation ability of titanium oxide semiconductors with optimized 1D morphology. Characterization techniques,

mainly Raman, X-ray photoelectron, and photoluminescence spectroscopies, clearly evidenced the in situ formation of SrTiO₃ domains on the surface of the Cu-doped TiO₂ nanotubes. Optimized formation in SrTiO₃ was found to be reached at a strontium loading of 0.8 wt% in Sr while further increase in Sr content to 1.0 wt% leads to the extra formation of SrO species partially covering the Cu-doped TiO₂ nanotubes. Correlation with photocatalytic evaluation in the degradation of formic acid shows that the formation in SrTiO₃ domains on the surface of Cu-doped TiO₂ nanotubes leads to enhanced photocatalytic performance with an optimum corresponding to the highest degree of formation in strontium titanate on the surface. Finally, the determination of dielectric properties strongly emphasizes that an optimum formation in SrTiO₃ helps to stabilize photogenerated charges at the semiconductor surface through in situ polarization effects probably induced by the ferroelectric properties of the adjacent SrTiO₃ surface domains. Further work is in progress in order to better deeply analyze the ferroelectric role of strontium in enhancing the photocatalytic properties of adjacent semiconductors.

Acknowledgement

The authors would like to acknowledge the fundings from Ministry of Education (IF-2020-019-BASRC) and Imam Abdulrahman Bin Faisal University, Basic and Applied Scientific Research Center obtained and Deputyship for Research & Innovation, Saudi Arabia (DSR-2019-087 Sci).

Cited references

- [1] L.M. Liu, Z. Chen, J.W. Zhang, D. Shan, Y. Wu, L.M. Bai, B.Q. Wang, *J. Water Process Eng.* 42 (2021) 102122.
- [2] M.H. Dalhat, A. Ahmad, in: *Development in Wastewater Treatment Removal and Process, Removal of Emerging Contaminants from Wastewater through Bionanotechnology*, chap. 19, Elsevier, 2022, pp. 435-458.
- [3] V.H. Nguyen, S. Meejoo Smith, K. Wantala, P. Kajitvichyanukul, *Arabian J. Chem.* 13 (2020) 8309-8337.
- [4] C.W. Huang, B.S. Nguyen, J.C.S. Wu, V.H. Nguyen, *Int. J. Hydrogen Energy* 45 (2020) 18144-18159.

- [5] J. Tian, Z. Zhao, A. Kumar, R.I. Boughton, H. Liu, *Chem. Soc. Rev.* 43 (2014) 6920–6937.
- [6] H. Zhao, P. Liu, X.X. Wu, A.G. Wang, D.W. Zheng, S.Y. Wang, Z.X. Chen, S. Larter, Y. Li, B.L. Su, *Appl. Catal. B* 291 (2021) 120055.
- [7] W.G. Wang, S.W. Liu, L.H. Nie, B. Cheng, J.G. Yu, *Phys. Chem. Chem. Phys.* 15 (2013) 12033-12039.
- [8] X.J. Zheng, L.F. Wei, Z.H. Zhang, Q.J. Jiang, Y.J. Wei, B. Xie, M.B. Wei, *Int. J. Hydrogen Energy* 34 (2009) 9033-9041.
- [9] A. Turki, H. Kochkar, C. Guillard, G. Berhault, A. Ghorbel, *Appl. Catal. B* 138-139 (2013) 401-415.
- [10] J. Tripathy, K. Lee, P. Schmuki, *Angew. Chemie Intl. Ed.* 53 (2014) 12605-12608.
- [11] H.B. Wu, H.H. Hng, X.W. Lou, *Adv. Mater.* 24 (2012) 2567-2571.
- [12] C.J. Li, G.R. Xu, B.H. Zhang, J.R. Gong, *Appl. Catal. B* 115 (2012) 201-208.
- [13] S. You, Y. Hu, X. Liu, C. Wei, *Appl. Catal. B* 232 (2018) 288–298.
- [14] Y. Cho, S. Kim, B. Park, C.L. Lee, J.K. Kim, K.S. Lee, I.Y. Choi, J.K. Kim, K. Zhang, S.H. Oh, *Nano Lett.* 18 (2018) 4257-4262.
- [15] R.C. Ding, Y.Z. Fan, G.S. Wang, *ChemistrySelect* 3 (2018) 1682-1687.
- [16] M. Niu, D.J. Cheng, D.P. Cao, *Sci. Rep.* 4 (2014) 4810.
- [17] M. Meksi, A. Turki, H. Kochkar, L. Bousselmi, C. Guillard, G. Berhault, *Appl. Catal. B* 181 (2016) 651-660.
- [18] H.Q. Sun, G.L. Zhou, S.Z. Liu, H.M. Ang, M.O. Tade, S.B. Wang, *Chem. Eng. J.* 231 (2013) 18-25.
- [19] G. Rossi, L. Pasquini, D. Catone, A. Piccioni, N. Patelli, A. Paladini, A. Molinari, S. Caramori, P. O'Keeffe, F. Boscherini, *Appl. Catal. B* 237 (2018) 603-612.
- [20] J. Lim, D. Monllor-Satoca, J.S. Jang, S. Lee, W. Choi, *Appl. Catal. B* 152 (2014) 233-240.
- [21] B. Xin, P. Wang, D. Ding, J. Liu, Z. Ren, H. Fu, *Appl. Surf. Sci.* 254 (2008) 2569-2574.
- [22] S. Sreekantan, S.M. Zaki, C.W. Lai, T.W. Tzu, *Mater. Sci. Semicond. Process.* 26 (2014) 620–631.
- [23] G. Colón, M. Maicu, M.C. Hidalgo, J.A. Navío, *Appl. Catal. B* 67 (2006) 41-51.
- [24] K. Lalitha, G. Sadanandam, V.D. Kumari, M. Subrahmanyam, B. Sreedhar, N.Y. Hebalkar, *J. Phys. Chem. C* 114 (2010) 22181-22189.

- [25] F. Dong, Z.Y. Wang, Y.J. Sun, W.K. Ho, H.D. Zhang, *J. Colloid Interf. Sci.* 401 (2013) 70-79.
- [26] M. Hamandi, G. Berhault, C. Guillard, H. Kochkar, *Appl. Catal. B* 209 (2017) 203-213.
- [27] S. Liu, J. Tian, L. Wang, Y. Luo, X. Sun, *Catal. Sci. Technol.* 2 (2012) 339-344.
- [28] P.D. Tran, S.K. Batabyal, S.S. Pramana, J. Barber, L.H. Wong, S.C.J. Loo, *Nanoscale* 4 (13) (2012) 3875-3878.
- [29] X.J. Lv, S.X. Zhou, C. Zhang, H.X. Chang, Y. Chen, W.F. Fu, *J. Mater. Chem.* 22 (2012) 18542-18549.
- [30] Y.F. Cui, J. Briscoe, S. Dunn, *Chem. Mater.* 25 (2013) 4215-4223.
- [31] W.G. Yang, Y.H. Yu, M.B. Starr, X. Yin, Z.D. Li, A. Kvit, S.F. Wang, P. Zhao, X.D. Wang, *Nano Lett.* 15 (2015) 7574-7580.
- [32] F. Wu, Y.H. Yu, H. Yang, L.N. German, Z.Q. Li, J.G. Chen, W.G. Yang, L. Huang, W.M. Shi, L.J. Wang, X.D. Wang, *Adv. Mater.* 29 (2017) 1701432.
- [33] X.Y. Huang, K.Q. Wang, Y.Z. Wang, B. Wang, L.L. Zhang, F. Gao, Y. Zhao, W.H. Feng, S.Y. Zhang, P. Liu, *Appl. Catal. B* 227 (2018) 322-329.
- [34] J. Zhang, J.H. Bang, C. Tang, P.V. Kamat, *ACS Nano* 4 (2010) 387-395.
- [35] E. Grabowska, M. Marchelek, T. Klimczuk, W. Lisowski, A. Zaleska-Medynska, *J. Catal.* 350 (2017) 159-173.
- [36] Q. Liu, Q. Sun, M. Zhang, Y. Li, M. Zhao, L. Dong, *Appl. Physics A* 122 (2016) 404 (5 pages).
- [37] T.K. Song, J. Kim, S.I. Kwun, *Solid State Comm.* 97 (1996) 143-147.
- [38] C. Ang, Z. Yu, Z. Jing, *Phys. Rev. B* 61 (2000) 957-961.
- [39] T.F. Nova, A.S. Disa, M. Fechner, A. Cavalleri, *Science* 364 (2019) 1075-1079.
- [40] S.T. Han, L.S. Yu, H.W. Zhang, Z.W. Chu, X.F. Chen, H.L. Xi, J.L. Long, *ChemCatChem* 11 (2019) 6203-6207.
- [41] Y. Watanabe, *Phys. Rev. B* 99 (2019) 064107.
- [42] S. Linic, P. Christopher, D. B. Ingram, *Nature Mater.* 10 (2011) 911-921.
- [43] Z. W. Seh, S. H. Liu, M. Low, S. Y. Zhang, Z. H. Liu, A. Mlayah, M. Y. Han, *Adv. Mater.* 24 (2012) 2310-2314.
- [44] C. Oubre, P. Nordlander, *J. Phys. Chem. B* 108 (2004) 17740-17747.
- [45] M. Meksi, H. Kochkar, G. Berhault, C. Guillard, *J. Molec. Catal. A* 409 (2015) 162-170.

- [46] M. Meksi, G. Berhault, C. Guillard, H. Kochkar, *Catal. Commun.* 61 (2015) 107-111.
- [47] H. Kochkar, N. Lakhdar, G. Berhault, M. Bausach, A. Ghorbel, *J. Phys. Chem. C* 113 (2009) 1672-1679.
- [48] E. Zghab, M. Hamandi, F. Dappozze, H. Kochkar, M. Saïd Zina, C. Guillard, G. Berhault, *Mater. Sci. Semiconductor Process.* 107 (2020) 104847.
- [49] D.V. Bavykin, J.M. Friedrich, F.C. Walsh, *J. Adv. Mater.* 18 (2006) 2807–2824.
- [50] F.B. Li, X.Z. Li, M.F. Hou, *Appl. Catal. B* 48 (2004) 185–194.
- [51] S. Meng, E. Kaxiras, *Nano Lett.* 10 (2010) 1238-1247.
- [52] J. Zhang, Z. Zhao, X. Wang, T. Yu, J. Guan, Z. Yu, Z. Li, Z. Zou, *J. Phys. Chem. C* 114 (2010) 18396-18400.
- [53] J. Nie, Y. Mo, B. Zheng, H. Yuan, D. Xiao, *Electrochim. Acta* 90 (2013) 589-596.
- [54] Y. Huo, J. Zhu, J. Li, G. Li, H. Li, *J. Molec. Catal. A* 278 (2007) 237-243.
- [55] L. Li, H. Zhuang, H. Bu, *Appl. Surf. Sci.* 257 (2011) 9221-9225.
- [56] L.Q. Jing, X.J. Sun, B.F. Xiu, B.Q. Wang, W.M. Cai, H.G. Fu, *J. Solid State Chem.* 177 (2004) 3375-3382.
- [57] D. Komaraiah, E. Radha, J. James, N. Kalarikkal, J. Sivakumar, M.V. R. Reddy, R. Sayanna, *J. Luminescence* 211 (2019) 320-333.
- [58] Q. Zhang, L. Gao, J. Guo, *Appl. Catal. B* 26 (2000) 207-215.
- [59] S. Liu, J. Tian, L. Wang, Y. Luo, X. Sun, *Catal. Sci. Technol.* 2 (2012) 339-344.
- [60] E. Morgado Jr., M.A.S. de Abreu, G.T. Moure, B.A. Marinkovic, P.M. Jardim, A.S. Araujo, *Chem. Mater.* 19 (2007) 665–676
- [61] F. Cesano, S. Bertarione, M.J. Uddin, G. Agostini, D. Scarano, A. Zecchina, *J. Phys. Chem. C* 114 (2010) 169–178.
- [62] J.C. Parker, R.W. Siegel, *Appl. Phys. Lett.* 57 (1990) 943-945.
- [63] M.J. Scepanovic, M. Grujic-Brojcin, Z.D. Dohcevic-Mitrovic, Z.V. Popovic, *Appl. Phys. A* 86 (2007) 365-371.
- [64] M.J. Scepanovic, S. Akrabic, V. Berec, A. Golubovic, Z.D. Dohcevic-Mitrovic, A. Kremenovic, Z.V. Popovic, *Acta Phys. Polonica A* 115 (2009) 771-774.
- [65] G. Colón, M. Maicu, M.C. Hidalgo, J.A. Navío, *Appl. Catal. B* 67 (2006) 41–51.
- [66] B. Ohtani, *J. Photochem. Photobiol. C* 11 (2010) 157-178.

- [67] M.S. Wrighton, A.B. Ellis, P.T. Wolczanski, D.L. Morse, H.B. Abrahamson, D.S. Ginley, J. Am. Chem. Soc. 98 (1976) 2774-2779.
- [68] P.W. Baumeister, Phys. Rev. 121 (1961) 359-363.
- [69] G. Busca, J. Mol. Catal. 43 (1987) 225-236.
- [70] H. Praliaud, S. Mikhailenko, Z. Chajar, M. Primet, Appl. Catal. B 16 (1998) 359-374.
- [71] C.H. Cao, L. Xiao, L. Liu, H.Y. Zhu, C.H. Chen, L. Gao, Appl. Surf. Sci. 271 (2013) 105-112.
- [72] M. Schiavoni, S. Campisi, P. Carniti, A. Gervasini, T. Delplanche, Appl. Catal. A 563 (2018) 43-53.
- [73] R. Hierl, H. Knözinger, H.P. Urbach, J. Catal. 69 (1981) 475-486..
- [74] B.R. Strohmeier, D.E. Leyden, R.S. Field, D.M. Hercules, J. Catal. 94 (1985) 514-530.
- [75] J.G. Yu, X.J. Zhao, Q.N. Zhao, Mater. Chem. Phys 69 (2001) 25–29.
- [76] D. Zhang, X. Ma, H. Zhang, Y. Liao, Q. Xiang, Mater. Today Energ. 10 (2018) 132–140.
- [77] K. Nagaveni, M.S. Hegde, N. Ravishankar, G.N. Subbanna, G. Madras, Langmuir 20 (2004) 2900–2907.
- [78] W. Zhao, K. Zhang, L.C. Wu, Q. Wang, D.H. Shang, Q. Zhong, J. Colloid Interf. Sci. 581 (2021) 76-83.
- [79] N.S. McIntyre, M.G. Cook, Anal. Chem. 47 (1975) 2208-2213.
- [80] M.P. Seah, in: D. Briggs, M.P. Seah (Eds.), Practical Surface Analysis, Wiley, 1990.
- [81] J. Ng, S. Xu, X. Zhang, H.Y. Yang, D.D. Sun, Adv. Funct. Mater. 20 (24) (2010) 4287–4294.
- [82] X.C. Lv, F.L.Y. Lam, X.J. Hu, Chem. Eng. J. 427 (2022) 131602.
- [83] Y. Bourlier, M. Frégnaux, B. Bérini, A. Fouchet, Y. Dumont, D. Aureau, Appl. Surf. Sci. 553 (2021) 149536.
- [84] N. Serpone, D. Lawless, R. Khairutdinov, J. Phys. Chem. 99 (1995)16646–16654.
- [85] J. Liu, J. Li, A. Sedhain, J. Lin, H. Jiang, J. Phys. Chem. C 112 (2008) 17127–17132
- [86] Y. Lei, L.D. Zhang, G.W. Meng, G.H. Li, X.Y. Zhang, C.H. Liang, W. Chen, S.X. Wang, Appl. Phys. Lett. 78 (2001) 1125–1127.
- [87] J. Preclikova, P. Galar, F. Trojanek, S. Danis, B. Rezek, I. Gregora, Y. Nemcova, P. Mały, J. Appl. Phys. 108 (2010) 113502.
- [88] Q.L. Xu, L.Y. Zhang, B. Cheng, J.J. Fan, J.G. Yu, Chem 6 (2020) 1543-1559.

- [89] S. Wageh, A.A. Al-Ghamdi, R. Jafer, X. Li, P. Zhang, *Chinese J. Catal.* 42 (2021) 667-669.
- [90] M.E. Guzhva, V.V. Lemanov, P.A. Markovin, W. Kleemann, *Phys. Solid State* 39 (1997) 618-624
- [91] D.P. Almond, A.R. West, *Solid State Ionics* 11 (1983) 57-64.
- [92] S. Komornicki, M. Radecka, M. Rekas, *J. Mater. Sci. Mater. Electron.* 12 (2001) 11–16.
- [93] J.B. Jorcin, M.E. Orazem, N. Pébère, B. Tribollet, *Electrochim. Acta* 51 (2006) 1473-1479.
- [94] N. Sdiri, H. Elhouichet, B. Azeza, F. Mokhtar, *J. Non-Crystall. Solids* 371-372 (2013) 22-27.

Figure Captions

Fig. 1. (A) XRD patterns of the xSr-0.5Cu-TiNT nanomaterials. Comparison to the copper-free TiNT (A), the strontium-free 0.5Cu-TiNT (B); xSr-0.5Cu-TiNT: C: 0.2 wt% Sr, D: 0.4 wt% Sr, E: 0.6 wt% Sr, F: 0.8 wt% Sr and G: 1.0 wt% Sr. (B) Zoom in the region of (101) anatase reflection showing the absence of shift effects with the addition of strontium.

Fig. 2. N₂ adsorption–desorption isotherms of the xSr-0.5Cu-TiNT nanomaterials. Comparison to the strontium-free 0.5Cu-TiNT. A: 0 wt% Sr, B: 0.2 wt % Sr, C: 0.4 wt% Sr, D: 0.6 wt% Sr, E: 0.8 wt% Sr and F: 1.0 wt% Sr.

Fig. 3. (A) Raman spectra of the xSr-0.5Cu-TiNT materials. Comparison to the strontium-free 0.5Cu-TiNT. A: 0 wt% Sr, B: 0.2 wt% Sr, C: 0.4 wt% Sr, D: 0.6 wt % Sr, E: 0.8 wt% Sr and F: 1.0 wt% Sr. (B) Zoom in the region of the E_{1g} active mode of anatase showing the presence of shift effects with the addition of strontium.

Fig. 4. UV–vis diffuse reflectance spectra of the xSr-0.5Cu-TiNT materials. Comparison to the strontium-free 0.5Cu-TiNT. A: 0 wt% Sr, B: 0.2 wt% Sr, C: 0.4 wt% Sr, D: 0.6 wt% Sr, E: 0.8 wt% Sr and F: 1.0 wt% Sr.

Fig. 5. SEM analysis of Sr-free 0.5Cu-TiNT (a and d), 0.6Sr-0.5Cu-TiNT (b and e), and 1.0Sr-0.5Cu-TiNT (c and f).

Fig. 6. A) XPS survey of the Sr-containing 0.2Sr-0.5Cu-TiNT, 0.6Sr-0.5Cu-TiNT and 1.0Sr-0.5Cu-TiNT samples with comparison to the Sr-free 0.5Cu-TiNT reference, B) examples of Ti 2p_{3/2} core-level spectra of the 0.5Cu-TiNT and 0.6Sr-0.5Cu-TiNT samples with fitting decomposition results into two contributions: Ti⁴⁺ (red) and Ti³⁺ (blue), C) examples of O 1 s core-level spectra of the 0.5Cu-TiNT and 0.6Sr-0.5Cu-TiNT samples with fitting decomposition results into two contributions: O_α (red) and O_β (blue), and D) Cu 2p core-level spectra of the Sr-containing 0.2Sr-0.5Cu-TiNT, 0.6Sr-0.5Cu-TiNT and 1.0Sr-0.5Cu-TiNT samples with comparison to the Sr-free 0.5Cu-TiNT reference. (For

interpretation of the references to colour in this figure legend, the reader is referred to the web version of this article.)

Fig. 7. Photoluminescence spectra of the series of $x\text{Sr}-0.5\text{Cu}-\text{TiNT}$ materials (with x in wt% Sr = 0.2, 0.4, 0.8 and 1.0).

Fig. 8. Photodegradation of FA in function of reaction time for the series of $x\text{Sr}-0.5\text{Cu}-\text{TiNT}$ materials (with x in wt% Sr = 0.2, 0.4, 0.8 and 1.0). Comparison to the Sr-free 0.5Cu-TiNT, TiNT and P25 as reference.

Fig. 9. Linear correlation between the initial rate of degradation of formic acid and the strontium amount added to the 0.5Cu-TiNT photocatalytic system.

Fig. 10. Nyquist diagrams acquired for the two low and high Sr-containing Cu-doped TiNT samples (0.2Sr-0.5Cu-TiNT and 0.8Sr-0.5Cu-TiNT) with corresponding fitting simulations and representation of the equivalent electric circuit.

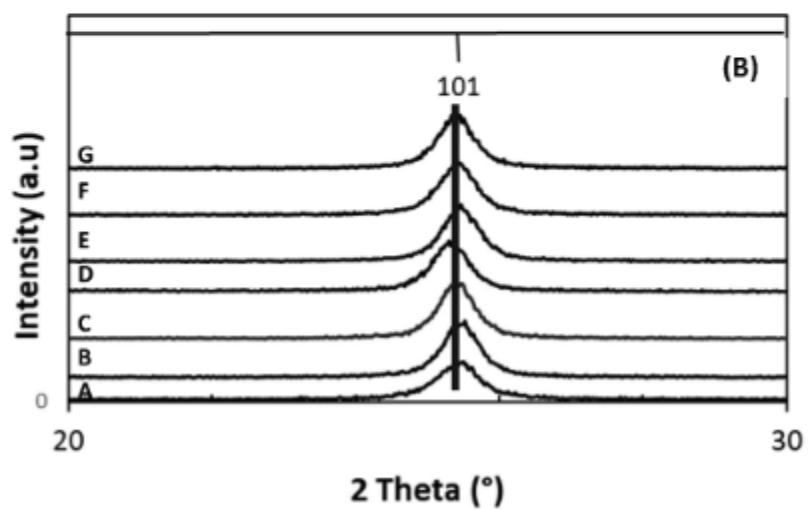
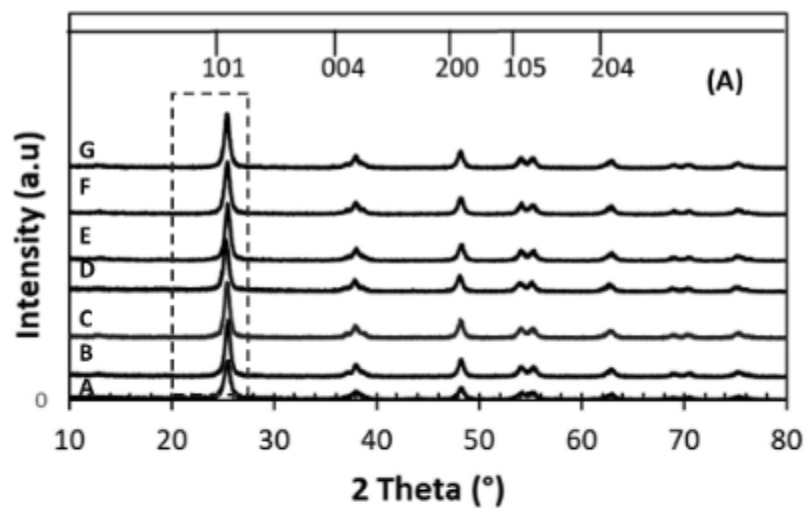


Figure 1

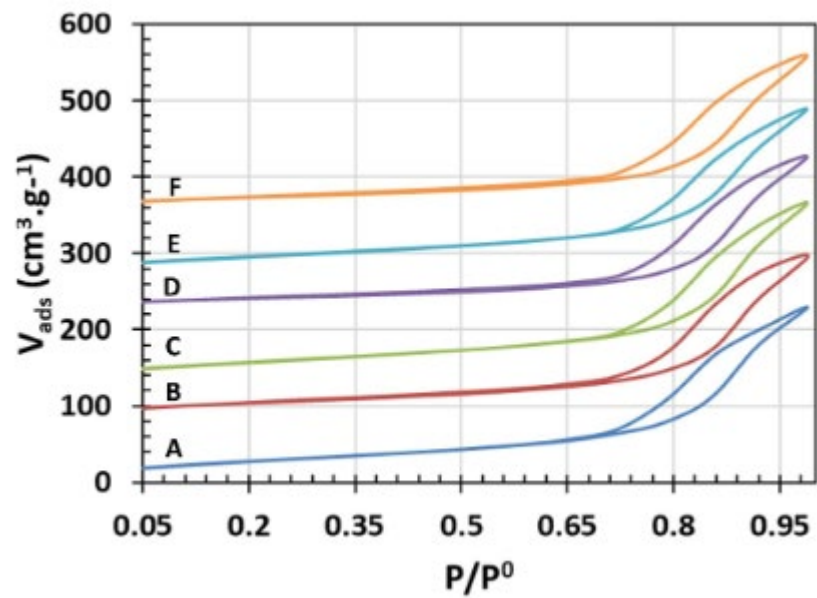


Figure 2

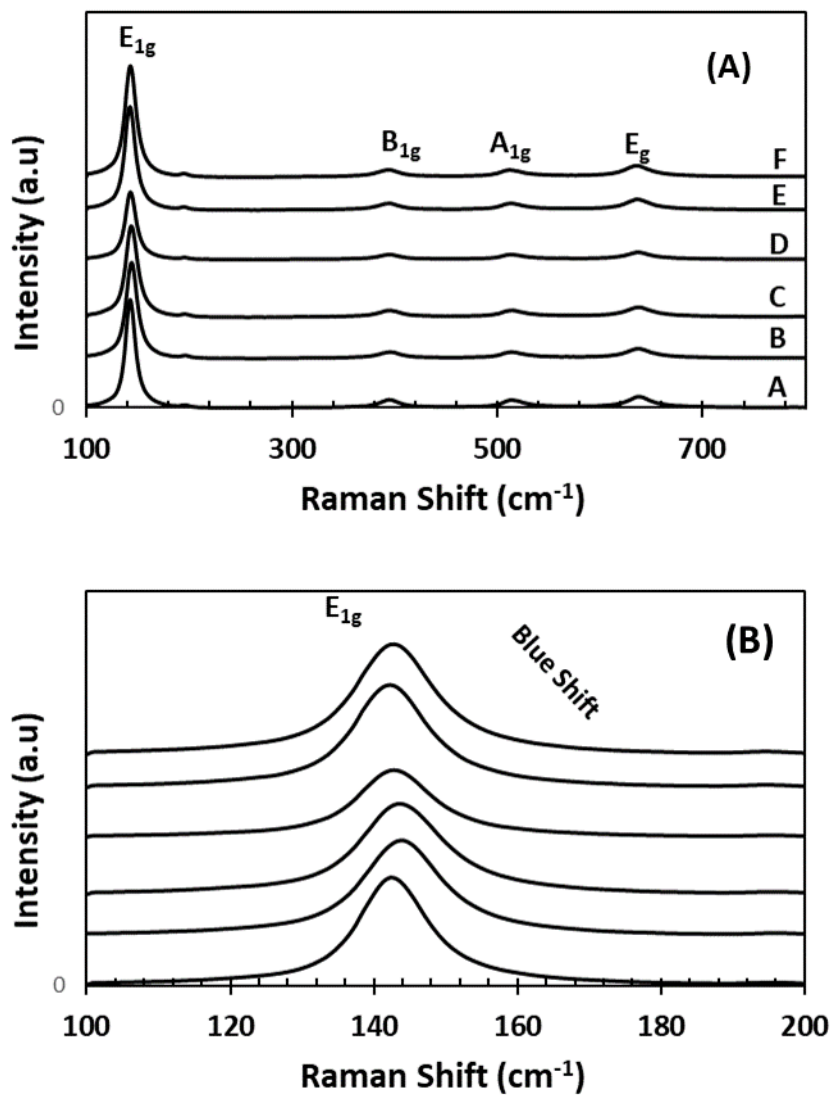


Figure 3

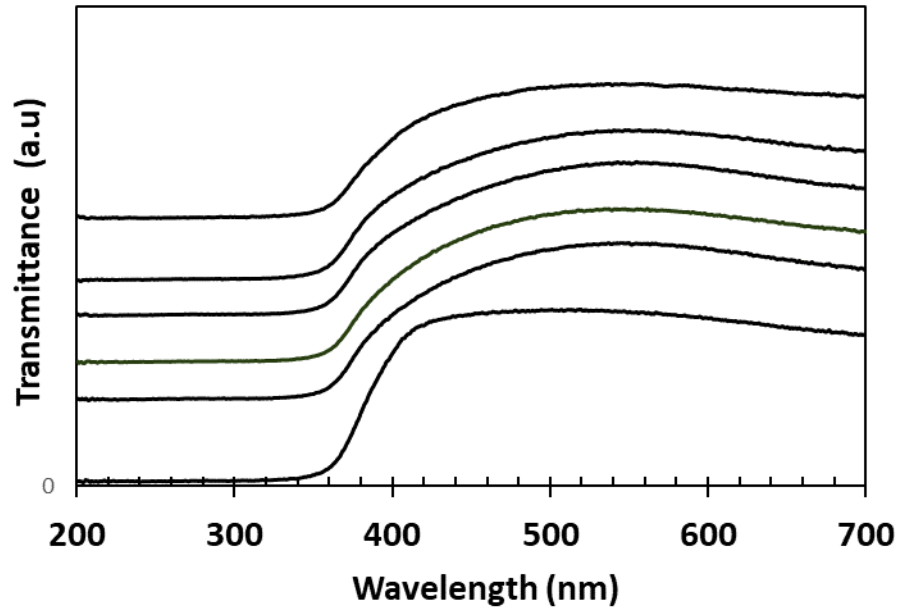


Figure 4

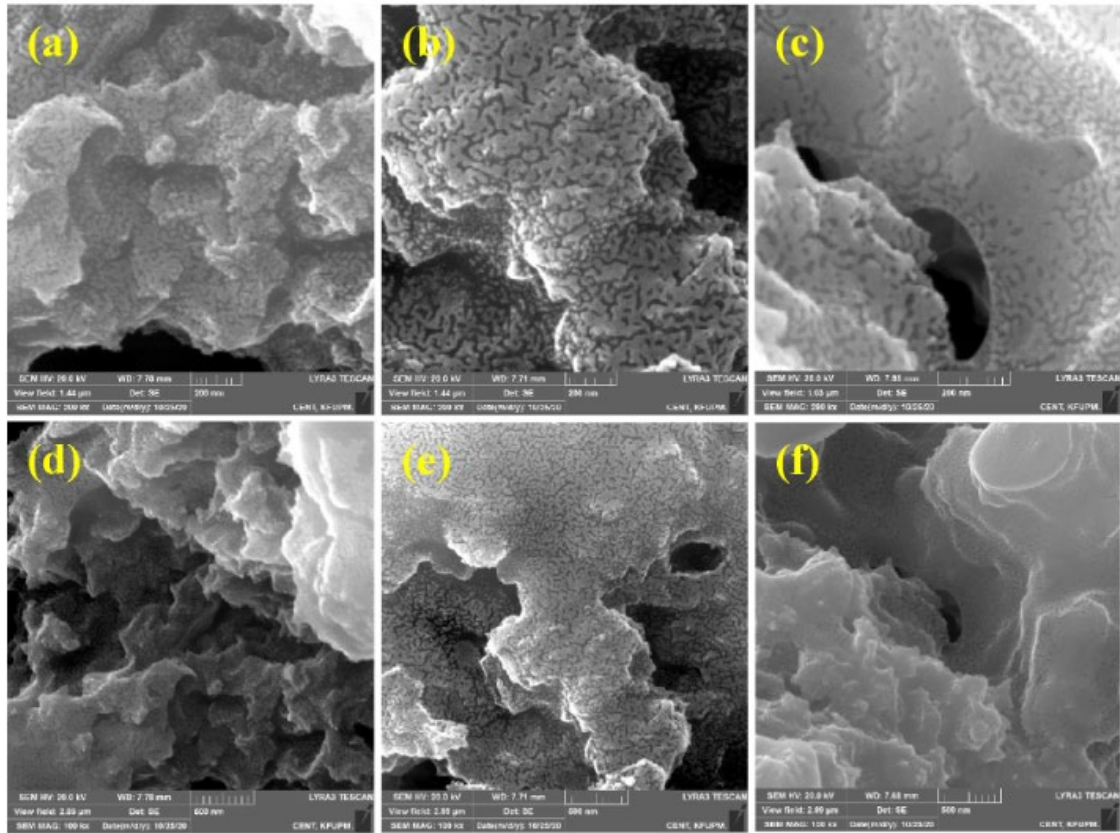
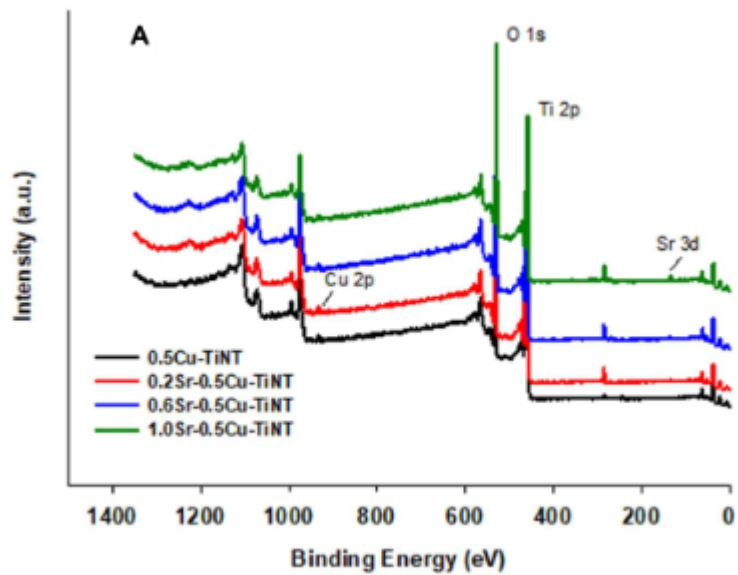


Figure 5



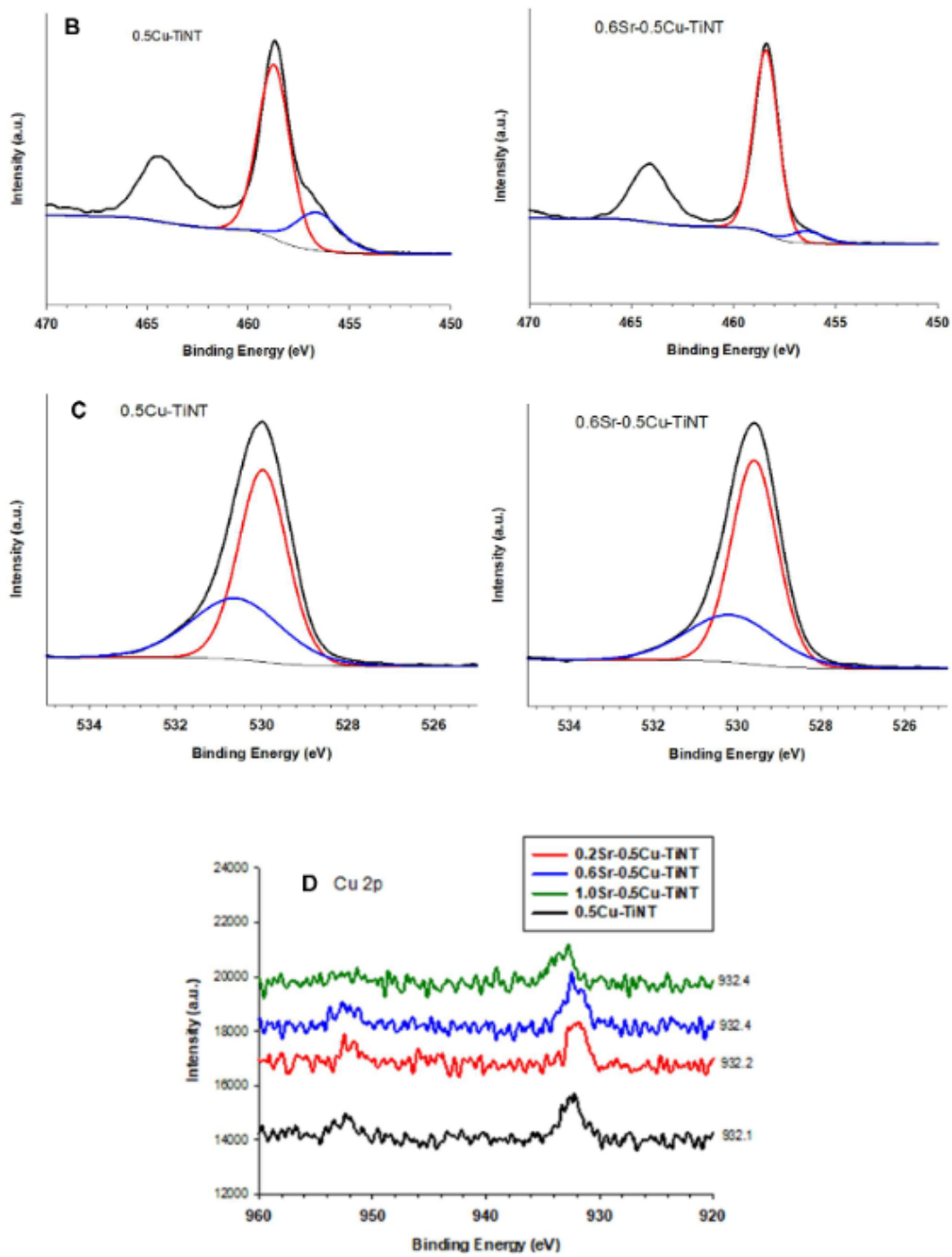


Figure 6

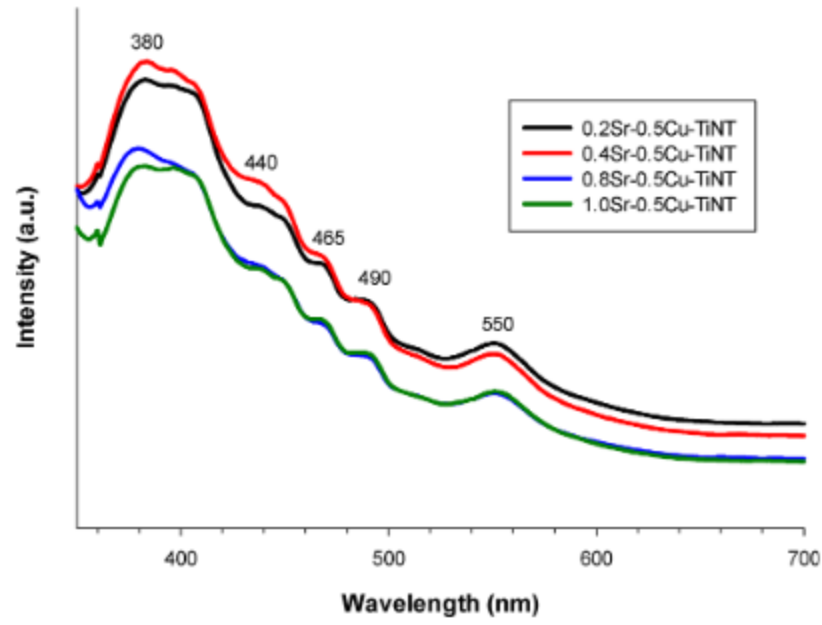


Figure 7

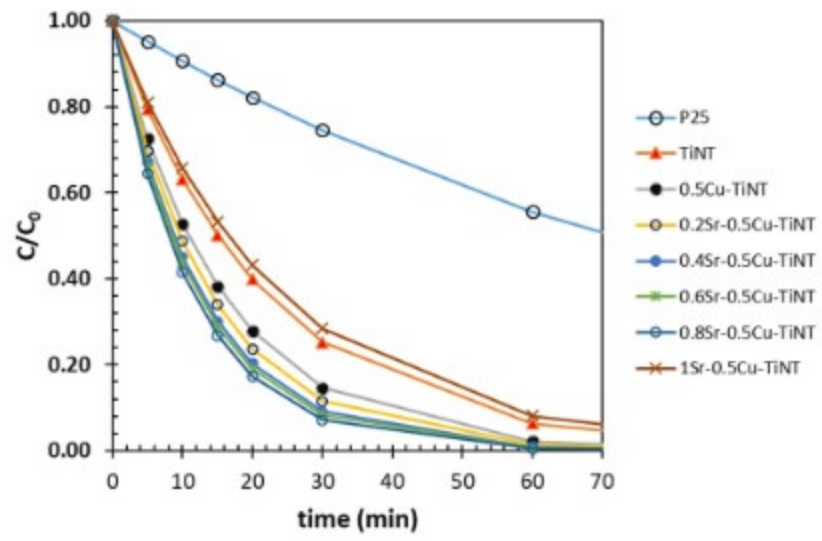


Figure 8

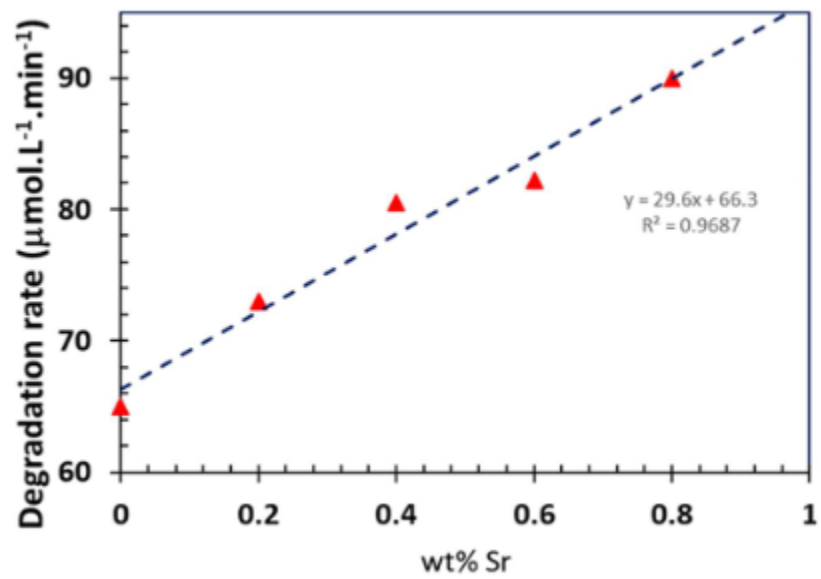


Figure 9

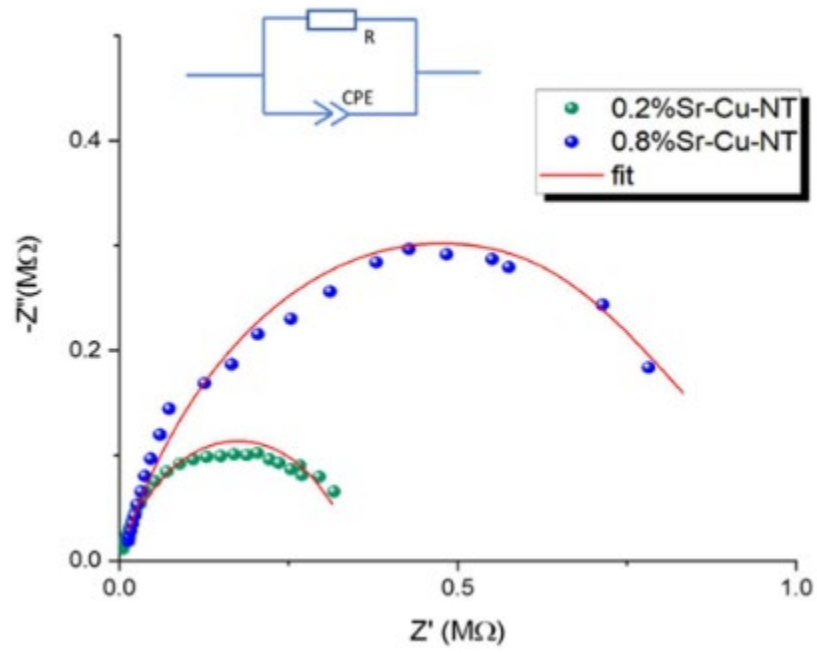


Figure 10

Table 1

ICP results reporting Cu and Sr loading on different samples of the xSr-0.5Cu-TiNT nanomaterials (x = in wt% = 0.2, 0.4, 0.6, 0.8 and 1). Comparison is provided with the strontium-free 0.5Cu-TiNT reference.

Amount wt%	Catalysts	
	Cu	Sr
–	0.48	0.5Cu-TiNT
0.22	0.47	0.2Sr-0.5Cu-TiNT
0.39	0.48	0.4Sr-0.5Cu-TiNT
0.61	0.49	0.6Sr-0.5Cu-TiNT
0.83	0.51	0.8Sr-0.5Cu-TiNT
1.15	0.48	1.0Sr-0.5Cu-TiNT

Table 2

Textural properties, anatase crystallite sizes and heat of N₂ adsorption of the xSr-0.5Cu-TiNT nanomaterials (x = in wt% = 0.2, 0.4, 0.6, 0.8 and 1). Comparison is provided with the strontium-free 0.5Cu-TiNT reference.

Heat of N ₂ adsorption (kJ.mol ⁻¹)*	Anatase Crystallite Size (nm)	E _g (eV)	V _p (cm ³ .g ⁻¹)	Pore Diameter (nm)	S _{BET} (m ² .g ⁻¹)	Catalysts
2.57	12.6	3.44	0.068	26.7	102	0.5Cu-TiNT
2.66	12.9	3.45	0.051	23.9	87	0.2Sr-0.5Cu-TiNT
2.65	12.8	3.45	0.062	24.4	84	0.4Sr-0.5Cu-TiNT
2.65	12.5	3.41	0.046	25.0	75	0.6Sr-0.5Cu-TiNT
2.68	12.2	3.41	0.057	24.3	72	0.8Sr-0.5Cu-TiNT
3.47	12.6	3.41	0.046	23.5	79	1.0Sr-0.5Cu-TiNT

* $C = \text{Exp} \left(\frac{E - EL}{RT} \right)$, with E: heat of N₂ adsorption onto catalyst and E_L heat of liquefaction of N₂ at 77 K

Table 3

XPS decomposition results of the Ti 2p_{3/2} and O 1s core-level spectra for the xSr-0.5Cu-TiNT samples (with x in wt% = 0.2, 0.6, 1.0) and comparison to the Sr-free 0.5Cu-TiNT reference. Binding energy values in eV and proportions in % (in parentheses) of each Ti and O species are indicated.

Samples	Ti 2p _{3/2}		O 1s	
	Ti ⁴⁺	Ti ³⁺	O _α	O _β
0.5Cu-TiNT	458.8 (76.2)	456.7 (23.8)	530.0 (63.0)	530.6 (37.0)
0.2Sr-0.5Cu-TiNT	458.6 (89.9)	456.8 (10.1)	529.7 (72.3)	530.4 (27.7)
0.6Sr-0.5Cu-TiNT	458.4 (91.8)	456.4 (8.2)	529.6 (69.0)	530.2 (31.0)
1.0Sr-0.5Cu-TiNT	458.3 (94.4)	456.4 (5.6)	529.5 (89.7)	531.0 (10.3)

Table 4

Photodegradation rate constant vs strontium loading on different samples of the xSr-0.5Cu-TiNT nanomaterials (x = in wt% = 0.2, 0.4, 0.6, 0.8 and 1). Comparison is provided with the strontium-free 0.5Cu-TiNT, the copper-free TiNT and P25 as reference. Experiments were triplicated.

Rate constant (k) μmol·L ⁻¹ ·min ⁻¹	Catalysts
35 ± 1	P25
46 ± 2	TiNT
64 ± 2	0.5Cu-TiNT
72 ± 4	0.2Sr-0.5Cu-TiNT
80 ± 5	0.4Sr-0.5Cu-TiNT
83 ± 5	0.6Sr-0.5Cu-TiNT
88 ± 3	0.8Sr-0.5Cu-TiNT
42 ± 1	1.0Sr-0.5Cu-TiNT

Table 5

The best fitting values of equivalent circuit elements for the low and high Sr-containing samples: 0.2Sr-0.5Cu-TiNT and 0.8Sr-0.5Cu-TiNT.

	R (kΩ)	A ₀ (10 ⁻¹⁰ F)	n	τ (μs)
0.2Sr-0.5Cu-TiNT	350	5.713	0.734	199.9
0.8Sr-0.5Cu-TiNT	948	3.748	0.722	355.3